Journal of Catalysis 384 (2020) 49–60

Contents lists available at ScienceDirect

Journal of Catalysis

journal homepage: www.elsevier.com/locate/jcat

The interplay between surface facet and reconstruction on isopropanol conversion over $SrTiO_3$ nanocrystals

Zhenghong Bao [a], Victor Fung [b,c], Felipe Polo-Garzon [a], Zachary D. Hood [d], Shaohong Cao [c], Miaofang Chi [c], Lei Bai [c,e], De-en Jiang [b], Zili Wu [a,c,*]

[a] Chemical Sciences Division, Oak Ridge National Laboratory, Oak Ridge, TN 37831, United States
[b] Department of Chemistry, University of California, Riverside, CA 92521, United States
[c] Center for Nanophase Materials, Oak Ridge National Laboratory, Oak Ridge, TN 37831, United States
[d] Department of Materials Science and Engineering, Massachusetts Institute of Technology, Cambridge, MA 02139, United States
[e] Department of Chemical and Biomedical Engineering, West Virginia University, Morgantown, WV 26506, United States

ARTICLE INFO

Article history:
Received 19 November 2019
Revised 13 February 2020
Accepted 14 February 2020
Available online 27 February 2020

Keywords:
Surface reconstruction
$SrTiO_3$
Isopropyl alcohol
Nanoshapes
Facet
SSITKA

ABSTRACT

Strontium titanate ($SrTiO_3$) is an extensively investigated perovskite for various applications due to its optical, electrical and chemical properties. To gain an in-depth understanding of the active sites involved in heterogeneous catalysis over the broadly used $SrTiO_3$ (STO), we studied a model reaction, isopropanol conversion, on three differently shape-controlled nanocrystals: cube, truncated cube and dodecahedra. SEM, XRD and XPS confirmed the morphology, phase and composition of STO shapes. Low energy ion scattering (LEIS) revealed the occurrence of surface reconstruction over STO shapes during O_2 pretreatment at different temperatures. Based on the catalytic activities, scanning transmission electron microscopy images and density functional theory calculations, the step sites on STO derived from surface reconstruction were proposed to be the active sites for isopropanol conversion. This was further confirmed by steady state isotopic kinetic analysis (SSITKA) which demonstrated similar intrinsic turnover frequencies (TOFs) for the differently reconstructed STO shapes. It is concluded that the crystal facets impose an indirect effect on the catalysis of STO via controlling the degrees of surface reconstruction: the less stable STO (1 1 0) facet (dodecahedra) leads to more step sites after reconstruction and hence higher overall reaction rate than the more stable (1 0 0) facet (cube). This work highlights the important interplay between the crystal facet and surface reconstruction in controlling the nature and density of active sties and thus catalysis over complex oxides.

1. Introduction

Perovskites are stable oxide materials with two cations and one anion in the formula of ABO_3. The cations A and B are tunable based on a criterion of $0.75 \leq t \leq 1.0$, where $t = (r_A + r_O)/[2^{0.5}(r_B + r_O)]$. Strontium titanate ($SrTiO_3$, STO) is an extensively investigated perovskite in various applications due to its physical [1–4] and chemical [5–9] properties. $SrTiO_3$ with a layer of $LaAlO_3$ could produce two-dimensional electron gas generated between their interfaces, inducing physical properties like ferromagnetism and/or superconductivity [10,11]. $SrTiO_3$-based photocatalysts can be used to effectively catalyze the overall water splitting and NH_3 synthesis via N_2 photofixation process [8,12].

Previously, our group has studied isopropyl alcohol (IPA) and ethanol conversions over STO nanocrystals. One major finding is that surface reconstruction of STO occurs readily and depends heavily on the pretreatment, posing a significant effect on catalysis. For example, Polo-Garzon et al. [13] used IPA conversion as a probe reaction over commercial STO perovskite revealed that the STO surface terminations could be controlled by surface reconstruction to tune the acid/base properties and thus the catalytic selectivity. Foo et al. [14] investigated the conversion of ethanol over a set of STO catalysts with different shapes, showing that dodecahedra STO (mainly (1 1 0) facet) has the highest ethanol dehydrogenation rate, followed by nitric acid etched cube, truncated ((1 0 0) + (1 1 0) facets), and cube STO ((1 0 0) facet). The ethanol turnover rate was related to the surface acid-base property as a result of the surface reconstruction of the different facets of STO nanocrystals [14].

* Corresponding author at: Chemical Sciences Division and Center for Nanophase Materials Sciences, Oak Ridge National Laboratory, Oak Ridge, TN 37831, United States.
E-mail address: wuz1@ornl.gov (Z. Wu).

https://doi.org/10.1016/j.jcat.2020.02.014
0021-9517/

These studies showed obvious surface reconstruction but the facet effect of STO on alcohol conversion remains unclear. Furthermore, there is a lack of information on (1) the true nature of the active sites for alcohol conversion, and (2) the true reaction rate in terms of turn over frequency (TOF) after the surface reconstruction. Recently, our work on methane combustion over a series of STO catalysts unveiled step sites at the surface after surface reconstruction as the active sites for methane activation and conversion [15]. This finding inspires us to re-visit alcohol conversion in order to understand the nature of active sites for acid-base reactions over STO perovskites.

For determination of the TOF of alcohol conversion over STO surfaces, we turn to steady state isotopic transient kinetic analysis (SSITKA) which is a powerful transient technique that could quantify important kinetic parameters which are inaccessible using common global kinetic studies, such as average surface residence times (τ), turnover frequencies, surface concentration (N), and surface coverage (θ) of the adsorbed reactant species and reaction intermediates [16–18]. A comprehensive view of SSITKA theory can be found in a review by Shannon et al. [19]. Researchers have extensively applied the SSITKA technique to study the reactions like ammonia synthesis [20,21], CH_4 activation [22,23], CO oxidation [24,25] and CO hydrogenation [26–28]. In contrast to metal surfaces, the quantification of the number of surface active sites required for achieving TOF values is quite challenging for oxide catalysts (especially under reaction conditions), where SSITKA is the desired technique.

In this work, we further explore the effects of both surface facet and reconstruction of the shape-controlled $SrTiO_3$ on the nature and quantity of active site using the isopropyl alcohol conversion as a probe reaction. Experimental investigation and theoretical calculation coupled with global and transient steady-state kinetics reveal that the minority step sites created by surface reconstruction are the active sites for IPA conversion. The starting STO facets are still important as they can be used to control the degree of surface reconstruction and consequently the catalysis. The results suggest that one cannot simply correlate the catalytic performance of complex oxides to their facets effect but should carefully investigate the surface reconstruction behaviors.

2. Experimental methods

2.1. Catalyst synthesis

The shape-controlled $SrTiO_3$ nanocrystals were prepared by the hydrothermal synthesis method with some modifications as reported previously [14,29]. Generally, the type of added solvent (DI water, ethanol, and pentaerythritol) determines the shape of $SrTiO_3$ nanocrystals (cube, truncated cube, and dodecahedra respectively). In detail, an ice bath using a 500-mL-glass trough was set up on a magnetic stirring stage. For the synthesis of STO cube, 20 mL DI water was added into a 150-mL-beaker located in the ice bath. 215 μL titanium chloride ($TiCl_4$, 99.9%, Sigma-Aldrich) was added dropwise into the beaker under a stirring of 400 rpm for 5 min, then add 24 mL 3 M $LiOH{\cdot}H_2O$ (>98% Sigma Aldrich) with a stirring for 30 min and add 8.1 mL 0.24 M $SrCl_2{\cdot}6H_2O$ (>99%, Alfa Aesar) followed by a stirring for another 30 min.

For the synthesis of truncated STO, 15 mL ethanol (200 proof, Decon Laboratories) was added into a 150 mL beaker located in the ice bath. 760 μL $TiCl_4$ was added dropwise into the beaker under a stirring of 400 rpm for 5 min. Subsequently, 38 mL of an aqueous solution of strontium chloride containing 1.855 g $SrCl_2{\cdot}6H_2O$ was added, stirred for 5 min, and then a 3.802 g NaOH tablet (99.1%, Fisher Scientific) was added with a vigorous stirring for 60 min.

For the synthesis of dodecahedra STO, 20 mL DI water was added into a 150 mL beaker located in the ice bath. 0.9623 g pentaerythritol and 215 μL $TiCl_4$ were added into the beaker under a stirring of 400 rpm for 5 min. Then 24 mL 3 M $LiOH{\cdot}H_2O$ was added with a stirring for 30 min and 8.1 mL 0.24 M $SrCl_2$ was added and stirred for another 30 min.

The resultant mixtures were transferred into 45 mL-teflon autoclaves (Parr 5000 Multi Reactor Stirrer System), heated to 180 °C and held for 48 h at a stirring rate of 800 rpm. After cooling to room temperature, the samples were centrifuged at 9000 rpm for 8 min. The collected samples were washed five times in deionized water and three times in ethanol. After drying the samples in a vacuum oven at 70 °C for 12 h, they were calcined in air at 550 °C for 4 h.

2.2. Characterizations

Powder X-ray diffraction (XRD) patterns were obtained using a PANalytical X'Pert Pro system with Cu Kα radiation at the conditions of 44 kV, 40 mA, and $2\theta = 10 - 90°$. Scanning electron microscopy (SEM) was performed using a Zeiss Merlin system operating at 1 kV.

Nitrogen physisorption was performed using a Micromeritics Gemini 2375 Surface Area and Pore Size Analyzer at −196 °C. Each sample was degassed at 300 °C for 1 h in an external furnace prior to the measurement. 17 points for the one-way P/P_0 varying were measured and the points between 0.05 and 0.3 on adsorption branch were used to calculate the BET surface area.

X-ray Photoelectron Spectroscopy (XPS) measurements were performed for STO shapes with/without additional ex situ calcination in O_2 at 550 °C for 5 h. XPS data were collected for each powder sample on a Thermo K-Alpha XPS system with a spot size of 400 μm and a resolution of 0.1 eV. All spectra were processed by use of Thermo Avantage, which is a software package provided through Thermo Scientific.

High-angle annular dark-field scanning transmission electron microscopy (HAADF-STEM) was carried out on an aberration-corrected Nion UltraSTEM-100 operated at 100 kV. Samples were drop-casted onto carbon-coated copper grids after dispersing each sample in ethanol. All images were taken after calcination of the samples at 550 °C for 5 h.

Low Energy Ion Scattering (LEIS) was performed at Lehigh University to determine the composition of the top surface layers. LEIS spectra were collected using an IONTOF Qtac^{100} spectrometer (Minster, Germany). Each sample was pressed at ~2000 psi with a protective piece of filter paper between the press and granules to create a pellet and transferred into a sample holder, which was then moved into a high-vacuum LEIS spectrometer system. Subsequently, LEIS analysis of the STO sample was performed from the top surface to 3 nm in depth using 3 keV He^+ as the probe ions at a size of 1.0 × 1.0 mm and a 1.0 keV Ar^+ for sputter-etching at a size of 1.5 × 1.5 mm area. The sample was then transferred to the LEIS preparation chamber where it was exposed to 100 mbar of O_2 at 550 °C for 5 h. After cooling to room temperature, the sample was transferred back into the spectrometer system for 0–3 nm profile analysis using the same conditions as before.

FTIR measurements were performed using a Thermo Nicolet Nexus 670 FTIR spectrometer. The nature of acid and base sites was determined by adsorbing pyridine and carbon dioxide, respectively, followed by FTIR spectroscopy. IPA adsorption and desorption at different temperatures were also performed to probe the surface interaction. Each spectrum was collected with 32 scans at a resolution of 4 cm^{-1}. Each catalyst was loaded into a porous ceramic cup, and the cup was inserted into a diffuse reflectance infrared Fourier transform spectroscopy (DRIFTS) cell (HC-900, Pike Technologies). The sample was pretreated at 550 °C for 1 h under 30 mL/min of 5% O_2/He and cooled to 25 °C in 30 mL/min of He.

During the cooling process, background spectra were collected at 300, 200, 150, 100 and 25 °C. For carbon dioxide adsorption, 30 mL/min of 2% CO_2/He was introduced into the DRIFTS cell at 25 °C for 10 min. Then, the sample was purged with 30 mL/ min of He for 10 min before a spectrum was collected at 25 °C. For pyridine and IPA adsorptions, 30 mL/min of He was bubbled through a saturator loaded with pyridine or IPA at 25 °C, and a pulse of saturated gas (0.5 mL) was introduced into the DRIFTS cell. A spectrum was collected after purging the cell for 15 min at 150 °C for pyridine adsorption. After the adsorption of IPA at 25 °C, a spectrum was collected at 100, 200 and 300 °C, and the appropriate background spectrum was subtracted accordingly.

Temperature programed oxidation (TPO) was performed over the used STO shapes to detect any potential carbon deposition from the reaction. After the activity test under the conditions of 250–300 °C and 0.5 μL/min IPA in 40 mL/min Ar (0.36% IPA in gas phase), the samples were purged in Helium (40 mL/min) at 100 °C for 0.5 h and then drop down to 25 °C. 40 mL/min 5% O_2/He was switched into the system and the temperature was increased from 25 to 600 °C at 10 °C/min. A quadruple mass spectrometer (ThermoStar GSD 300) was used to monitor the response of CO_2 in the tail gas. To quantify the amount of CO_2 generated during TPO and hence the carbon deposition, 20 pulses (507 μL/pulse) of 1% CO_2/Ar-He were calibrated using the same mass spectrometer right before the TPO measurement.

Steady state isotopic transient kinetic analysis (SSITKA) experiments were carried out on a home-made system [23,30]. The masses recorded with respect to time in the mass spectrometer were 20-Ne, 40-Ar, 39-Propene, 58 and 60 for Acetone. The transient switch experiments were performed using labeled isopropanol-1,3-$^{13}C_2$ (Sigma-Aldrich). Firstly, the regular IPA in carrier gas of 2%Ne/98%He was flowed through the catalyst bed at 280 °C. After reaching steady state, the feed gas was switched to the labeled reactant (IPA-1,3-$^{13}C_2$/2%Ar/98%He) while continuously monitoring the masses of interest using a quadruple mass spectrometer (OmniStar GSD 320). To obtain the real mean surface residence times (τ_0 = extrapolation of τ to zero point) [31,32], four gas hourly space velocities (GHSVs) were used at 45, 60, 120, 240 $L{\cdot}g^{-1}{\cdot}h^{-1}$. The gas-phase hold-up time for the SSITKA system was determined using the diluted Ne tracer in He gas, which is the integration of the area of Ne in the normalized transient response graph. The calculation of SSITKA parameters for IPA conversion on STO shapes was detailed in supporting information (Cal. S1).

To determine the strength and concentration of IPA adsorption sites on STO shapes and STO dodecahedra sample at different pretreatment temperatures (550, 750 and 900 °C), the chemisorption of IPA was performed using a Micromeritics 3Flex Characterization Analyzer coupled with a Setaram Sensys Evo DSC microcalorimeter [33]. Each sample was evacuated at 30 °C for ~1 h, and then heated up to 550 °C at 7 °C/min under 500 mmHg of O_2. Once at 550 °C, the sample was maintained under O_2 for ~2.7 h, evacuated for 30 min, exposed to 500 mmHg of O_2 for 2.3 h, and finally evacuated for 2.5 h. The temperature of the sample was then reduced to 30 °C while evacuating. Once 30 °C was reached and thermal equilibrium was attained, IPA was dosed to perform the measurements. After the final target pressure was reached, the sample was evacuated for 1 h at 30 °C and IPA was dosed again. The repeat-run was performed to calculate the number of irreversible adsorption sites. In 750 and 900 °C cases, an extra calcination in air was performed right before loading the sample in the microcalorimeter.

2.3. IPA conversion evaluation

The catalytic activities for IPA conversion over STO shapes were performed using an Altamira Instruments system (AMI-200). Each catalyst (0.020 g, 60–80 mesh) was diluted with quartz (0.200 g, 60–80 mesh) to minimize channeling and local temperature differences. The catalyst bed was placed inside a quartz u-tube and held in place by placing quartz wool at both ends of the bed. Each sample was pretreated under 40 mL/min of 10% O_2/Ar at 550 °C for 5 h. The temperature was lowered to designated temperature, and the catalytic performance was measured in a temperature rising sequence. The feed gas was switched to 0.5 μL/min of IPA and 40 mL/min of Ar (0.36% IPA in gas phase). Liquid IPA was fed into the system using a Chemyx Nexus 3000 syringe pump. Products were analyzed using a Buck Scientific Model 910 gas chromatograph (GC) equipped with a flame ionization detector and a Restek MXT-Q-BOND column. The GC response factor was calibrated using various of compositions of 2-propanol, acetone and propene. All lines were heated to 110 °C to prevent condensations of reactant and products.

2.4. DFT calculations

The density functional theory calculations were performed using the Vienna Ab Initio Simulation Package (VASP) [34,35]. The Perdew-Burke-Ernzerhof (PBE) [36] functional form of generalized-gradient approximation (GGA) was used for electron exchange and correlation energies. Dispersion corrections were added using the D3 method by Grimme [37]. The projector-augmented wave method was used to describe the electron-core interaction [34,38]. A kinetic energy cutoff of 450 eV was used. All calculations were performed with spin polarization. The Brillouin zone was sampled using a Monkhorst-Pack scheme with a $3 \times 3 \times 1$ grid [39]. A vacuum layer of 15 Å was used for the surface slabs along the z-direction and the atoms in the bottom two layers were fixed during the calculations. Transition states (TS) were found with the nudged elastic band (NEB) [40] and the dimer method [41] using a force convergence criterion of 0.05 eV/Å.

3. Results and discussions

3.1. Morphology and surface properties

Fig. 1 shows the SEM images of $SrTiO_3$ nanocrystals with different shapes. The STO_Cube has a cubic morphology with an average side length of 300 nm, which is bounded by (1 0 0) facets (Fig. 1A). The morphology of truncated $SrTiO_3$ nanocrystals (~200 nm) is cubic with its edges truncated by (1 1 0) facets (Fig. 1B), with an estimated truncation of 50%. The truncation degree is the ratio between the area of (1 1 0) and the areas of (1 0 0) and (1 1 0) facets, based on more than 50 particles. For dodecahedra STO, the nanocrystals have a mean particle size of ~150 nm and a high degree of truncation (>95%), resulting in a dodecahedron shape with predominantly the (1 1 0) facets being exposed (Fig. 1C). By carefully comparing the three shapes based on the particle dimensions, the sizes of (1 0 0) and (1 1 0) facets on Truncated STO are 11% and 45% of that on Cube and Dodecahedra samples, respectively. The STO nanocrystals calcinated at high temperature of 900 °C resulting in more truncation and particle sintering (see Fig. S1).

XRD patterns of STO Cube, Truncated, and Dodecahedra are given in Fig. S2. All samples displayed the pure phase of strontium titanate (JCPDS#86–0179). Each sample showed major peaks at 22.8, 32.5, 40.1, 46.6, 57.9, 67.9, and 77.5° which are assigned to the (1 0 0), (1 1 0), (1 1 1), (2 0 0), (2 1 1), (2 2 0), and (3 1 0) planes of the cubic crystal structure of STO, respectively.

XPS was used to detect the surface composition of STO shapes. The quantification of each element is shown in Table 1. Peak fittings are displayed in Fig. S3. Generally, the Sr/(Sr + Ti) ratio of all samples is around 0.5. There is a trace amount of Na element

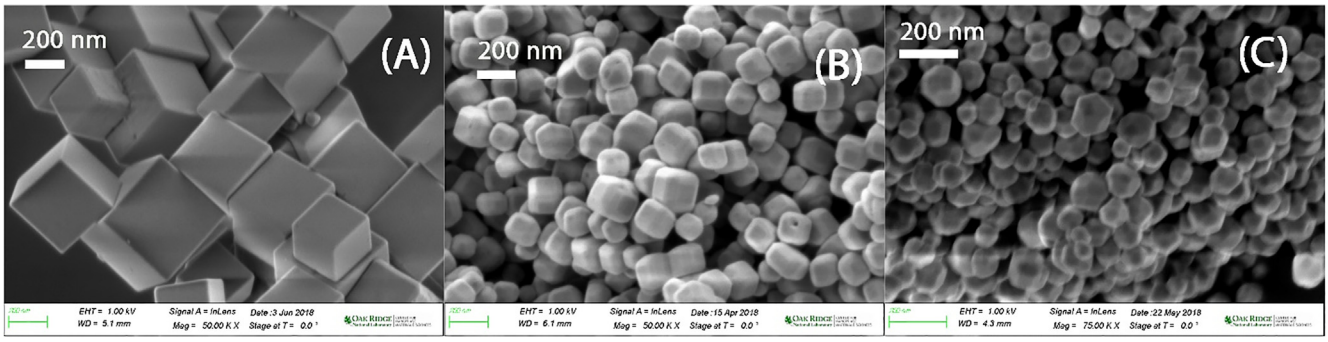

Fig. 1. SEM images of $SrTiO_3$ nanocrystals with different shapes calcinated at 550 °C. (A) cube, (B) truncated, and (C) dodecahedra.

Table 1
XPS results of STO shapes measured with/without thermal treatment in O_2 for 5 h.

Sample	Atomic percentage (%)						
	Sr	Ti	O	Na	Cl	Li	Sr/(Sr + Ti)
Truncated_NT[a]	18.0	19.7	59.5	2.8	0	0	0.48
Cubes_NT	18.1	20.3	60.0	1.7	0	0	0.47
Dodecahedra_NT	18.4	20.2	60.2	1.2	0	0	0.48
Truncated_550C	18.6	19.2	59.8	2.4	0	0	0.49
Cubes_550C	18.4	20.6	59.4	1.6	0	0	0.47
Dodecahedra_550C	19.1	19.8	60.1	1.1	0	0	0.49

[a] NT denotes no treatment.

in the samples which may come from the impurity of reagents. But the commonly used elements Cl and Li in the precursors were not detected, indicating the wash step was complete. After thermal treatment in O_2, the averaged Sr/(Sr + Ti) ratio has a slightly increase, indicating a Sr enrichment at the STO surface within ~3 nm (XPS measurement depth). The enrichment is not obvious because the probing depth of XPS does not allow for characterization of top surface layers with monolayer sensitivity which can be obtained via low energy ion scattering as shown below. From the results of SEM, XRD and XPS, we demonstrate that the as-synthesized STO shapes are pure in bulk perovskite structure with surface enrichment of Sr after calcination, similar to our previous observations of these STO [14,15].

Compared to XPS, low energy ion scattering (LEIS) is more surface sensitive and therefore more suitable to determine the composition of top atomic layers on the STO samples [14,42]. Fig. 2A and B show the ratio of Sr/(Sr + Ti) on the STO shapes as a function of probing depth using LEIS technique (see LEIS spectra in Fig. S4). Prior to calculating the surface ratio, the intensity of each cation was normalized to unity at the largest depth (3.5 nm). LEIS measurements for the STO samples without thermal pretreatment (Fig. 2B) showed that the Sr/(Sr + Ti) ratios for all three shapes increased with probing depth and finally arrived at ~0.5, which represents the bulk composition. Cube has a low Sr/(Sr + Ti) ratio of 0.25 at the first few angstroms, while that for Truncated and Dodecahedra samples are around 0.45, indicating surface enrichment of Ti. After pretreatment at 550 °C for 5 h in oxygen (same as the pretreatment condition used before the IPA reaction test), the top surfaces of all three shapes are enriched with Sr cations as shown in Fig. 2A. Thus, the surface composition of STO shapes changed from Ti-enrichment to Sr-enrichment after the thermal treatment due to surface reconstructing [13,15]. Consequently, an amorphous SrO moiety as indicated by previous STEM imaging [13,15], rather than massive phase separation, was formed on the

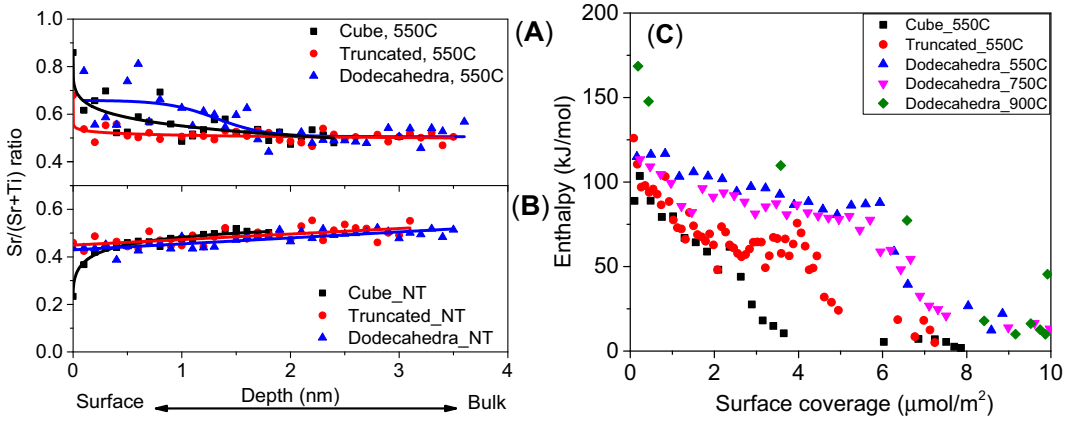

Fig. 2. Surface Sr/(Sr + Ti) cation intensity ratio as a function of probing depth using LEIS for STO shapes: with treatment at 550 °C (A) and without treatment (B). Heat of adsorption of isopropyl alcohol on STO shapes measured at 30 °C (C).

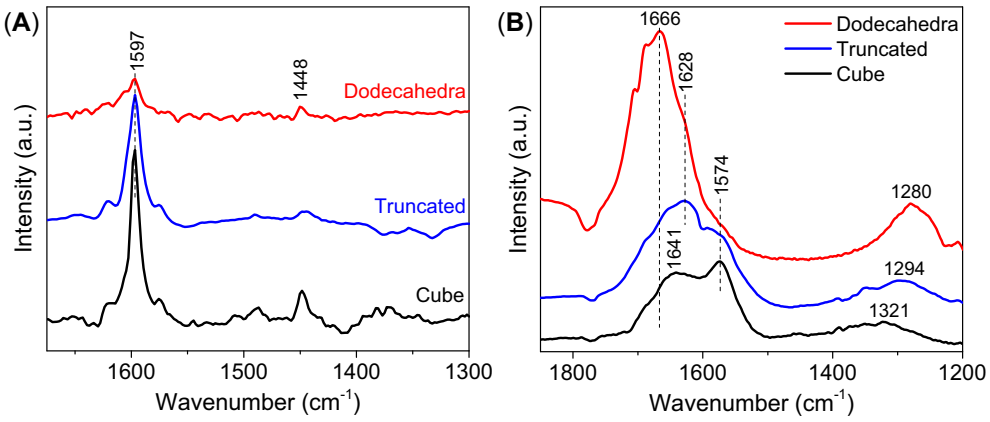

Fig. 3. FTIR spectra of (A) pyridine adsorption at 150 °C and (B) CO_2 adsorption at 25 °C on STO shapes.

STO surface due to no pure SrO phase shown in XRD pattern. The lack of peaks at 1444–1520 cm^{-1} in CO_2 DRIFTs (Fig. 3 below) suggests no bulk $SrCO_3$ in the STO perovskite, indirectly approving no buck SrO in the STO shapes. STO Cube has the most variation in outmost surface composition: the Sr/(Sr + Ti) ratio changes from 0.25 without pretreatment to 0.85 with treatment.

Table 2 shows the surface area of different STO shapes obtained from N_2 physisorption. After calcination at 550 °C, STO cube has the lowest surface area, followed by Truncated and Dodecahedra samples. This trend is in accordance with the particle size observed in SEM images (Fig. 1): larger particles result in smaller surface areas. The dodecahedra sample was additionally tested after thermal treatment in 5%O_2/Ar atmosphere at 750 and 900 °C, showing a decreasing trend in BET surface area.

Adsorption microcalorimetry experiments were conducted to measure the strength and density of surface sites accessible for IPA adsorption at 30 °C. From Fig. 2C, the heat of adsorption generally decreases with the increase of surface coverage for all STO samples. The distribution of adsorption sites for IPA on Cube and Truncated STOs are similar up to 2.5 μmol/m^2, above which they show some difference. The dodecahedra sample always displays a different distribution of adsorption sites for IPA compared to the other two shapes. The adsorption strength of IPA, characterized by the heat of IPA adsorption, is higher on dodecahedra STO than on cube and truncated samples for the whole range of surface coverage. Dodecahedra treated at 900 °C shows the strongest adsorption of IPA. For the STO shapes activated at 550 °C, the density of adsorption sites follows the trend of cube < truncated < dodecahedra. Treating the dodecahedra at 550, 750 and 900 °C does not affect the density of sites for IPA adsorption, despite the change of the surface area (Table 2).

To determine the nature of acid and base sites, FTIR spectra were recorded for the adsorption of pyridine and CO_2 on the STO shapes (Fig. 3). The peaks observed in Fig. 3A at 1448 and 1597 cm^{-1} are ascribed to pyridine coordinated to surface Lewis acid sites [43,44]. Based on the relative intensity of peak 1597 cm^{-1}, the cube sample shows highest density of Lewis acid sites, followed by truncated and dodecahedra samples. The absence of the typical IR band at ~1540 cm^{-1} suggests the absence of Bronsted acid sites on the STO shapes.

Interaction of CO_2 with weakly basic hydroxyl groups, medium and strong basic surface oxygen atoms over metal oxides results in the formation of bicarbonate, bidentate and unidentate carbonates, respectively [14]. Upon adsorption of CO_2, broad peaks with shoulders are observed at around 1600 cm^{-1} for all three STO samples, but the difference among them is also obvious (Fig. 3B). The major peaks observed at 1574 cm^{-1} on Cube, 1628 cm^{-1} on Truncated and 1666 cm^{-1} on Dodecahedra can be assigned to the asymmetric vibration of unidentate carbonate [14], asymmetric stretching of bicarbonate [29] and asymmetric vibration of bidentate carbonate [45], respectively. Dodecahedra STO has the largest density of Lewis basic sites because of its highest relative intensity at around 1600 cm^{-1}, followed by truncated and dodecahedra samples. The peak at 1321 cm^{-1} on STO Cube is assigned to a $SrCO_3$ species caused by the adsorption of CO_2 on an amorphous SrO moiety of the STO surface [29,46]. The amorphous SrO moiety forms after pretreatment at 550 °C in the presence of O_2 as verified by LEIS in Fig. 2A. The bands at 1280 cm^{-1} on dodecahedra and 1294 cm^{-1} on truncated catalysts are both attributed to the symmetric vibration of bidentate carbonate [45]. Absence of IR peaks at 1444–1520 cm^{-1} range for all three samples indicates there is no bulk $SrCO_3$ in the STO perovskite [29], which agrees well with the XRD results.

Table 2
Surface area of $SrTiO_3$ nanocrystals and surface density of sites accessible by IPA at 30 °C.

Catalyst	BET surface area (m^2/g)	Surface sites density (μmol/m^2)
Cube_550C	6.9	2.8
Truncated_550C	9.8	4.4
Dodecahedra_550C	12.8	6.4
Dodecahedra_750C	8.8	6.5
Dodecahedra_900C	7.1	5.9

3.2. In situ FT-IR

Fig. 4 shows the FTIR spectra of IPA adsorbed on the $SrTiO_3$ shapes. For pure *iso*-propyl alcohol, the peak at 1466 cm^{-1} is attributed to the asymmetric δCH_3 vibration, while the two peaks at 1390 and 1375 cm^{-1} are assigned to the symmetric δCH_3 vibration. The peak at 1290 cm^{-1} is associated with δOH vibration [47,48]. Peaks shown at 1163, 1132, and 1097 cm^{-1} are ascribed to νC—C, ρCH_3, and νC—O vibrations, respectively [49]. Table S1 summarizes the peak assignments. Some changes are observed when IPA is adsorbed on the STO shapes at 25 °C. The most obvious one is that the peak at 1097 cm^{-1} (νC—O) for all three samples disappeared, which is possibly shifted to higher wavenumbers and merged with the peak at 1132 cm^{-1} upon adsorption and dissociation of IPA to isopropoxy on the STO surfaces [50]. The peak at 1132 cm^{-1} on STO shapes has a slightly shift to the lower wavenumber direction. In addition, the relative intensity of the peak at 1163/1132 cm^{-1} for Dodecahedra, Truncated and Cube decreased, increased and kept

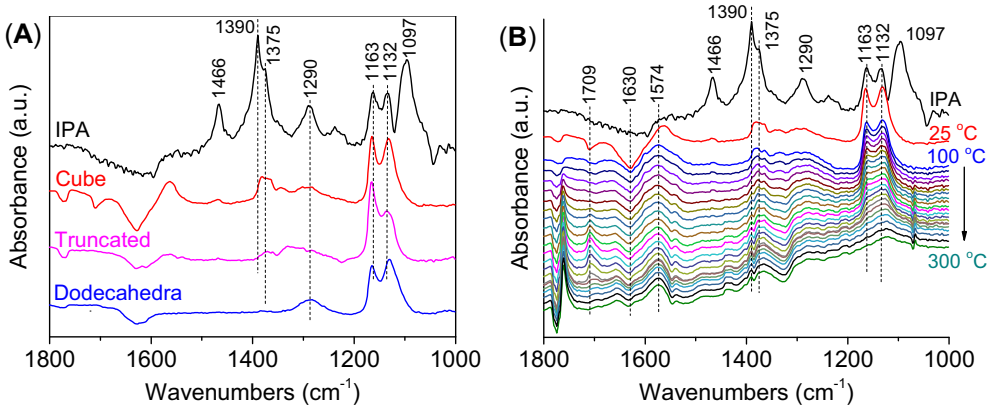

Fig. 4. FTIR spectra (A) of IPA adsorption on STO shapes at 25 °C, and (B) collected during temperature-programmed reaction (25–300 °C) of IPA on STO Cube.

the same, respectively, suggesting that the oxygen atom of IPA interacts with the STO facets to different extents.

After the adsorption of IPA at RT, the temperature was ramped at 10 °C/min under flowing Argon to observe the surface reaction of IPA. Only the FTIR spectra for temperature-programmed reaction of IPA on STO cube is shown here in Fig. 4B, since the results are similar on truncated and dodecahedra samples (Fig. S5). At 25 °C, an obvious negative peak is observed at 1630 cm^{-1} on the STO cube (Fig. 4B), which can be attributed to the release of water molecules [49]. As the temperature was increased from 25 to 300 °C, the peaks at 1466, 1290, 1163 and 1132 cm^{-1} gradually decreased in intensity and then vanished, indicating the reaction/desorption of the alcohol group. Meanwhile, two new peaks emerged at 1709 and 1574 cm^{-1}, which are due to the νC=O and νC=C vibrations of acetone and propene, respectively [49], suggesting the occurrence of surface reaction of adsorbed IPA. The intensity of the peak at 1709 cm^{-1} increased first and then decreased with the temperature, probably due to the desorption of the adsorbed acetone species.

All three STO samples show the νC=O peak at ~1709 cm^{-1}, coupled with the experimental observation of high acetone selectivity (Fig. 5) and literature results [13,50–53], we can infer a reaction pathway including acetone formation and desorption on the catalyst surface as follows: initially, the H atom in the alcohol group adsorbed on a basic surface oxygen atom. Then, a surface OH group is formed by breaking the original isopropanol O—H bond, and the rest of the isopropoxy is adsorbed on an adjacent Lewis acid site (metal atom in STO). Finally, another surface oxygen atom abstracts the alpha H atom to form an acetone molecule and the combination of two OH groups gives a H_2 molecule.

3.3. IPA conversion reactivity

IPA conversion over STO samples displayed a good stability based on a time-on-stream running at 320 °C for at least 10 h (Fig. S6). The carbon balance is ~100% due to the negligible carbon deposition on the catalyst after reaction based on the TPO characterization (Fig. S7). When the STO samples were tested for IPA reaction in the temperature range 250–300 °C (Fig. 5), the IPA conversions and reaction rates (based on surface area) for all samples increased as a function of reaction temperature. The dodecahedra sample had the highest reaction rate based on unit surface area, followed by the cube and truncated samples. According to LEIS measurement, pretreatment at 550 °C caused surface reconstruction of the STO shapes. Therefore, it appears that the reconstructed (1 1 0) facet has a higher activity than the reconstructed (1 0 0) facet. Truncated STO has the lowest reactivity per surface area, an observation not understood at this point and will be discussed later on. The acetone selectivity for cube and dodecahedra keeps almost constant over the examined reaction temperatures, while for truncated sample it decreases from 92% to 78% (Fig. 5B), which could be explained from the activation energy point of view. Apparent activation energy (E_a) for acetone formation is very similar on the three STO samples (87–95 kJ/mol) while the E_a for propene formation over truncated STO (148 kJ/mol) is much larger than the other two STO samples (119 and 112 kJ/mol for cube and dodecahedra, respectively) (Fig. S8). Larger E_a will lead to faster increase of rate than smaller E_a with the increase of reaction temperature, thus higher selectivity to propene (lower selectivity to acetone) was observed on truncated sample with the reaction temperature ramping.

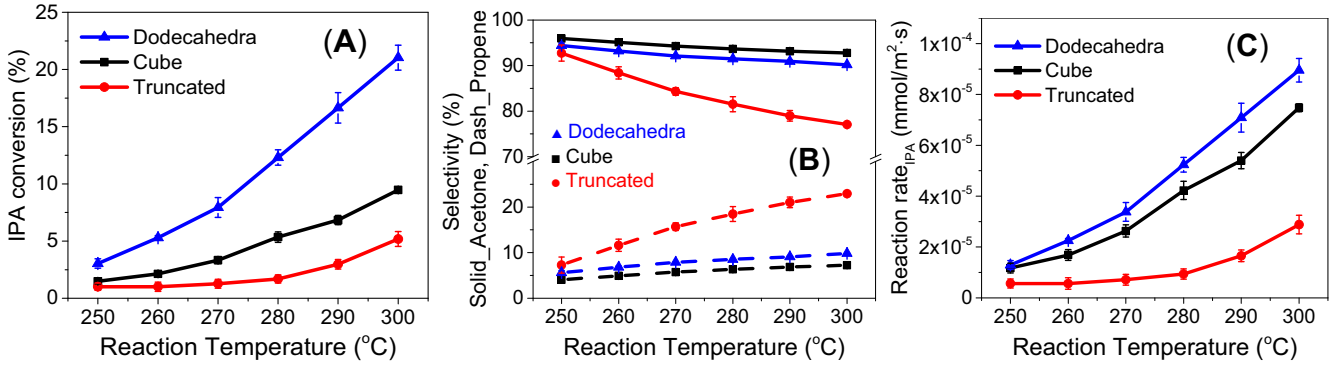

Fig. 5. Steady state conversion (A), selectivity (B), and reaction rate (C) of IPA dehydrogenation/dehydration over STO shapes. Reaction conditions: 250–300 °C, and 0.5 μL/min IPA in 40 mL/min Ar (0.36% IPA in gas phase).

Since pretreatment temperature and time have an effect on the catalytic conversion of IPA and methane combustion over commercially obtained STO [13,15], the effect of pretreatment temperature on IPA conversion over the samples synthesized in the present work was studied. Due to the highest rate per surface area, the (1 1 0) dominated dodecahedra sample was selected to further investigate the effect of different pretreatment temperatures. When there was no thermal treatment (NT) performed on the dodecahedra sample, IPA conversion and consumption rate were the lowest (Fig. 6A, C). The reaction rate increased with the pretreatment temperature (Fig. 6C). The propene selectivity for thermal treated samples increases with the increase of pretreatment temperature (Fig. 6B), although it only varies in a limited extent (5–15%). Higher pretreatment temperature has shown to round the STO cubes and generate some steps and facets with higher Miller index, resulting in higher catalytic activity in methane combustion over STO [15]. Here, similar mechanism could be applicable for STO dodecahedra mainly containing (1 1 0) facet, which is verified by Scanning Transmission Electron Microscopy (see in Fig. 7). The STEM image in Fig. 7A shows a clear dodecahedra shape for the dodecahedra sample at a lower magnification, and in Fig. 7B represents the selected area in Fig. 7A at a higher magnification. A further enlargement of the selected area showing step sites is displayed in Fig. 7C, in which the brighter and larger sphere is Sr and the darker and smaller ball is Ti element. The atoms arrangement matches well with the model (1 1 0) facet in the insertion of Fig. 7C. The STEM images for cube and truncated STOs have been provided in our previous publications [13,15]. Due to the extreme low activity of the sample without pretreatment, it appears that the thermal-induced higher-indexed facets, i.e., the step sites, are related to the enhanced activity in IPA conversion. Therefore, we propose the active sites for IPA conversion are the step sites created by surface reconstruction during the thermal pretreatment, which will be quantified and elaborated by the following SSITKA studies and DFT calculations.

It is worth to note in Fig. 6B that all pretreated dodecahedra samples have a much lower propene selectivity at 300 °C than that of the sample without pretreatment. This is caused by the reconstruction of the STO surface: the surface Sr/(Sr + Ti) ratio increased when the sample was treated in oxygen at elevated temperatures (See in Fig. 2A), leading to surfaces with more enriched Sr^{2+} termination and more basic sites, and thus lower propene selectivity. IPA conversion on pure SrO directs to the formation of acetone, while on pure TiO_2 leads to propene [13].

3.4. Steady-state isotopic transient kinetic analysis (SSITKA)

SSITKA was applied to acquire the information about the catalyst-surface reaction intermediates. The normalized transient mass spectrometry responses of products for IPA conversion at 280 °C over the three STO shapes at different GHSVs after a switch from regular IPA to labeled IPA-1,3-$^{13}C_2$ are shown in Fig. 8. Since the major product is acetone from IPA conversion over the STO samples and the rate-determining step was shown to be the alpha-H abstraction [13] and thus the labeling of the 1,3-carbon of IPA would pose minimal impact on the reaction kinetics and hence can be used for SSITKA study here. The average surface residence time (τ) of a species is the integration of the area between the normalized transient responses of the species and that of Neon tracer gas. As shown in Fig. 8, τ for propene and acetone decreased with increasing GHSV, indicating the products re-adsorbed readily on the surface of STO shapes. If the reaction species did not re-adsorb, τ would be independent from GHSV [32]. The response of propene and acetone are similar; thus, one could suggest that propene and acetone share a common intermediate during the IPA conversion over STO shapes. The common intermediate here

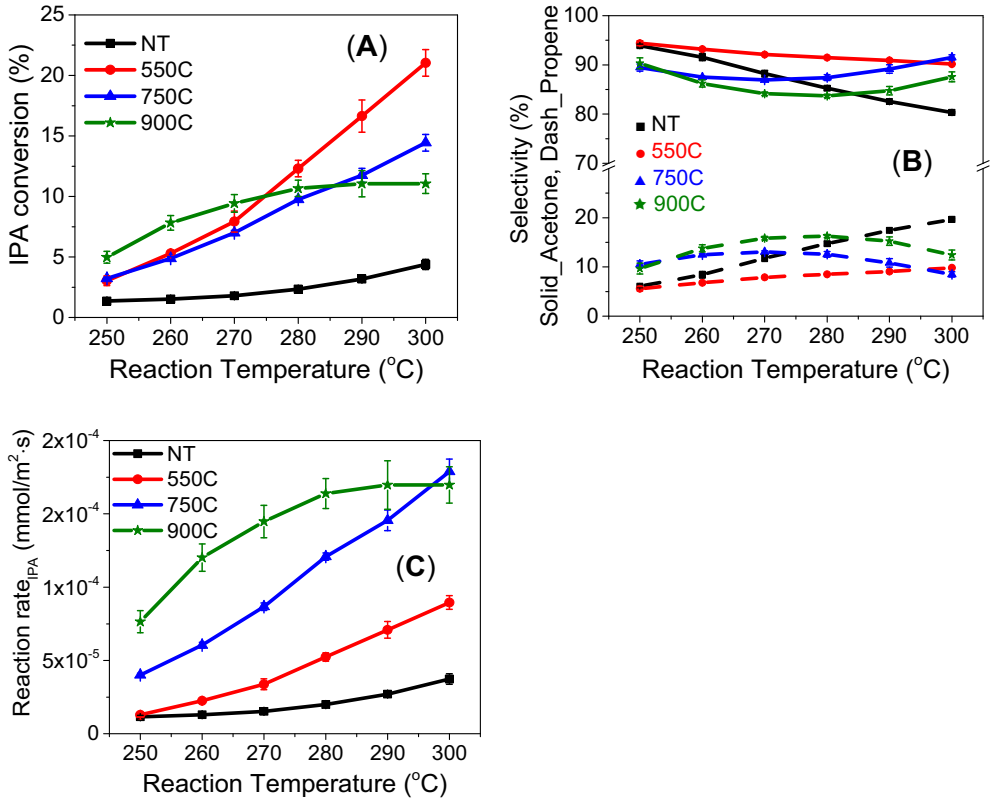

Fig. 6. Conversion (A), selectivity (B), and reaction rate (C) of IPA conversion over dodecahedra STO pretreated at different conditions. Reaction conditions: 250–300 °C and 0.5 μL/min IPA in 40 mL/min Ar (0.36% IPA in gas phase).

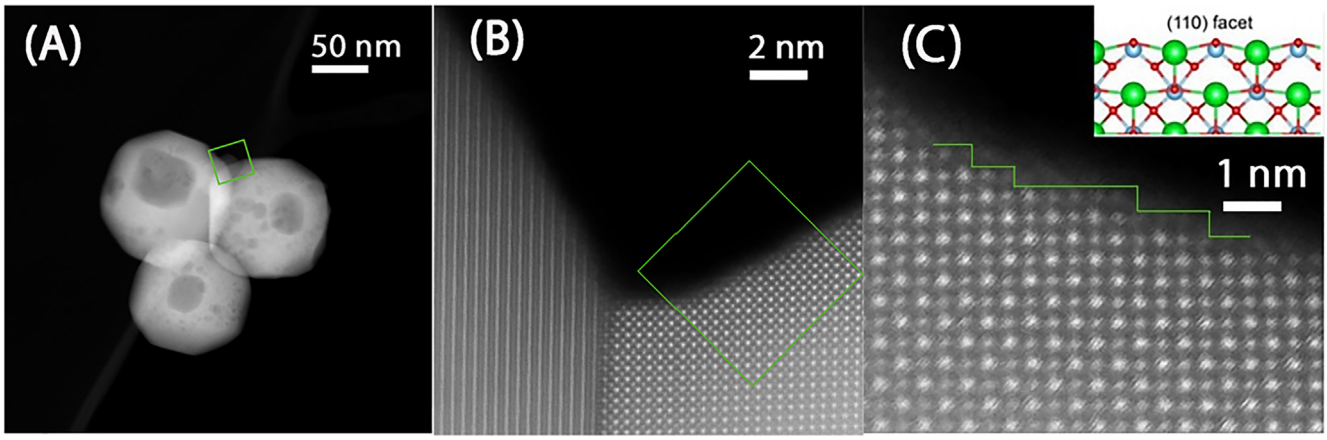

Fig. 7. HAADF-STEM images of STO Dodecahedra pretreated at 550 °C for 5 h in oxygen. (A) lower magnification of dodecahedra sample, (B) higher magnification, (C) Steps on (1 1 0) facet, insertion is the model of (1 1 0) facet (Elements: Red, oxygen; Green, Sr; Blue, Ti).

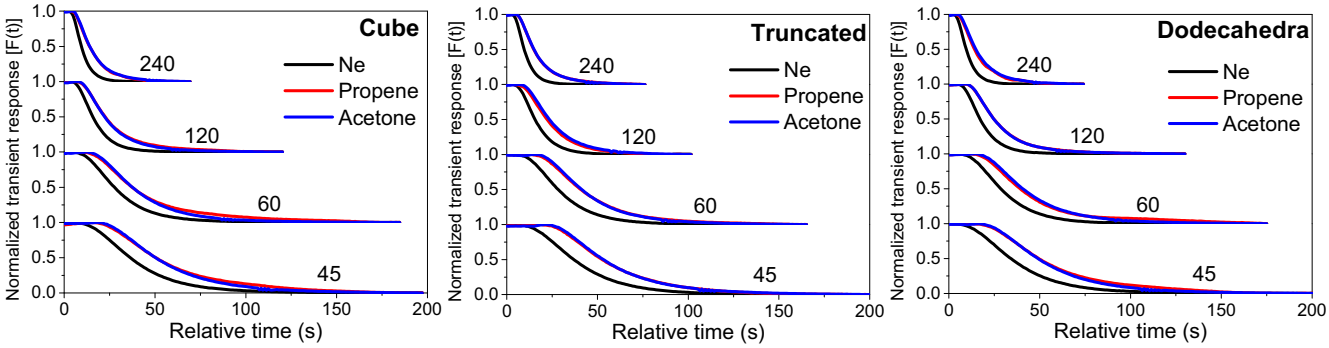

Fig. 8. Normalized transient responses of the decay curve for reactant gas switch from regular IPA to IPA-1,3-$^{13}C_2$ over STO shapes at 280 °C and different GHSVs (45–240 $L{\cdot}g^{-1}{\cdot}h^{-1}$).

is isopropoxy, as suggested by *in situ* FTIR (Fig. 4) and the following DFT calculations. The average surface residence times derived from Fig. 8 are summarized in Table S2.

By using the data in Table S2, an extrapolation line can be drawn to obtain the real mean surface residence time (τ_0) of reaction intermediates at zero contact time or infinite GHSV (Fig. 9). Several parameters can be derived from τ_0, such as turn over frequency (TOF), concentration of surface intermediates (N), and coverage of surface intermediates (θ). The calculation formulas are presented in supporting information Cal. S1, and the results are listed in Table 3. SSITKA experiments were also conducted on STO dodecahedra pretreated at different temperatures. The integration of areas to get average surface residence times, extrapolation to acquire the real mean surface residence times and the calculated SSITKA parameters are shown in Fig. S9-10, Table S3 and Table 3, respectively.

From Table 3, all the STO shapes show a similar TOF, suggesting the same type of active sites over the different STO samples for IPA conversion. The TOFs obtained from three different methods are compared in Fig. 10. Clearly, the TOF determined by isotopic labeling technique (TOF_{SSITKA}, see Cal.S1) is the largest among the ones defined by rate per theoretical active site ($TOF_{theoretic}$, see in Cal. S2 for the calculation of theoretical active site) and by rate per accessible site via IPA adsorption measured in the microcalorimetry

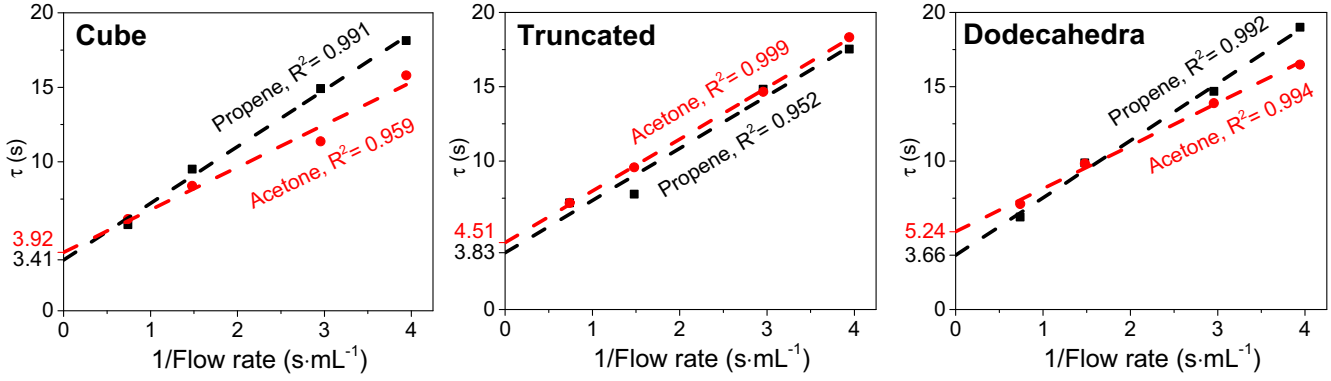

Fig. 9. Real mean surface residence times (τ_0) of reaction intermediates over STO shapes at 280 °C obtained by extrapolating the average surface residence times (τ) at different contact times of 3.94, 2.96, 1.48 and 0.74 s mL^{-1} (by varying GHSV) to zero contact time.

Table 3
Summary of the real mean surface residence time (τ_0, s), TOF, concentration of surface intermediates and surface coverage at 280 °C.

STO Catalysts	τ_0 (s)		TOF (s^{-1})[a]		Concentration of surface intermediates (mol/m^2)[b]		Coverage of surface intermediates (%)[c]	
	Propene	Acetone	Propene	Acetone	Propene	Acetone	Propene	Acetone
Cube_550C	3.4	3.9	0.29	0.26	9.14×10^{-9}	1.55×10^{-7}	0.04	0.73
Truncated_550C	3.8	4.5	0.26	0.22	6.63×10^{-9}	3.45×10^{-8}	0.03	0.16
Dodecahedra_550C	3.7	5.2	0.27	0.19	1.63×10^{-8}	2.51×10^{-7}	0.07	1.11
Dodecahedra_750C	3.7	3.6	0.26	0.27	5.61×10^{-8}	3.84×10^{-7}	0.17	1.17
Dodecahedra_900C	4.2	4.1	0.24	0.24	1.11×10^{-7}	5.61×10^{-7}	0.27	1.38

[a] TOF = $1/\tau_0$.
[b] Concentration of surface intermediates = Steady-state reaction rate (280 °C) * τ_0.
[c] Coverage of surface intermediates = Concentration of surface intermediates * $100/((C_{t1} + C_{t2})/S_{BET})$.

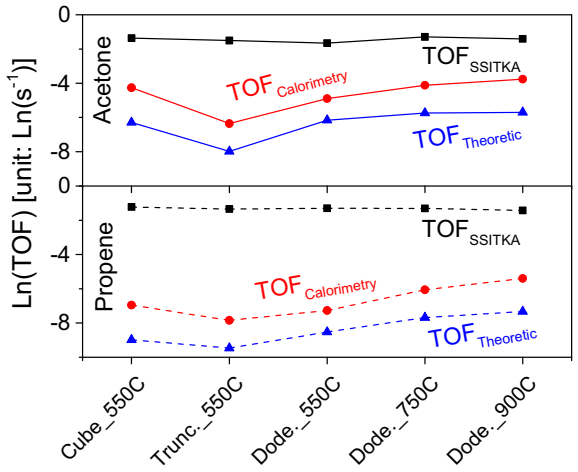

Fig. 10. A comparison of different TOFs for STO shapes after different calcination temperatures.

($TOF_{Calorimetry.}$). TOF_{SSITKA} is a more accurate measure of the turnover frequency per active intermediate, as the measurement is performed at steady-state reaction conditions. $TOF_{theoretic}$ is the lowest value because not every surface site (anion and cation sites) used in the calculation acts as the actual active site. The $TOF_{Calorimetry}$ is between the two other TOFs because the number of surface sites titrated by IPA adsorption at 30 °C is much larger than the real number of actives, but smaller than that from the theoretical surface sites. When it comes to the concentration and coverage of surface intermediates for the tested samples, the dodecahedra sample shows the highest concentration and coverage of surface intermediates, followed by cube and truncated STOs. This trend is similar to the activity trend in Fig. 5. The high coverage of surface intermediates seems to be responsible for the high global reactivity of IPA conversion over STO dodecahedra, since TOF is similar for all samples. In turn, the higher surface coverage means the higher density of active sites on the catalyst surface assuming a one-by-one adsorption pair of active sites and intermediates. It is notable that even the highest surface coverage of intermediate is<1.4% on the 900 °C treated STO dodecahedra, indicating that a very small portion of the surface sites on the STO is actually active for the conversion of IPA. Such small numbers further support that the step sites derived from the reconstruction are responsible for the IPA reaction over STO.

3.5. DFT calculations

To model the reconstruction of a complex-oxide surface is still challenging from first principles. Here we adopted an alternative approach by using a high-index surface, STO (4–10) (equivalent to the (4 1 0) facet in a cubic perovskite system) that resembles the reconstructed surface based on high-angle annular dark-field scanning transmission electron microscopy [15]. Given the partially reducing conditions during IPA conversion, a reduced (4–10) STO surface with its step sites (Fig. S11) was used in their DFT calculations to understand the IPA conversion mechanisms. The energies for adsorption and intermediates are listed in (Table S4) in the SI. We focus our scope on the O-H dissociation and the rate-limiting C-H activation of IPA on the surface.

We found that IPA first adsorbs non-dissociatively on the flat (1 0 0)-like Sr-O sites (Fig. 11, structure a) or dissociatively on the Ti sites at the edge (Fig. 11, structure c and c′). The dissociation of the O—H bond proceeds from the Fig. 11a state to the Fig. 11b transition state with a barrier of 0.06 eV and then to Fig. 11c stable state with a downhill energy change of −1.2 eV. Following O—H dissociation, the isopropoxy intermediate can be converted to propene or acetone via the cleavage of either the C_β—H or C_α—H bond, respectively (Fig. 11, structure d, d′). Cleaving the C_α—H bond leads to a CH_3COCH_3 moiety (Fig. 11, structure e) on the surface which can desorb to form acetone by the cleaving of the O—Ti bond. Meanwhile cleaving the C_β—H bond will form a CH_3CHOCH_2 moiety (Fig. 11, structure e′) which can desorb to form propene by the cleaving of the C—O bond. We found the cleavage of the C_α—H bond and the desorption of the acetone (the acetone pathway in Fig. 11) to be kinetically favored over the cleavage of the C_β—H bond which is in good agreement with the higher experimental acetone selectivity. Furthermore, the rate-limiting C—H activation barrier was found to be 1.08 eV which is also in good agreement with the experimental barriers (~100 kJ/mol). Compared to the (1 0 0) surface from our previous DFT study using the same methods [13], IPA was both found to adsorb more strongly (−2.34 eV vs −1.40 eV) and have lower C—H activation energies (1.08 eV vs 1.54 eV) on the edge sites. The stronger adsorption can be attributed to the cooperative attraction of the Ti and the Sr sites with the oxygen of isopropoxy at the edges. Meanwhile, the lower C—H activation energy is likely due to the stronger H abstraction ability of the undercoordinated edge oxygen. These results are in agreement with the observed increased activity of the $SrTiO_3$ nanoparticles that are calcinated at higher temperatures with higher concentrations of these active step sites. Step defects were reported to be more active than simple surfaces in many different reactions [54–56]. In addition, the energy profile in Fig. 11 confirms the proposed reaction mechanism based on the *in situ* FITR observations in Fig. 4.

3.6. General discussion on facet effect vs surface reconstruction

The results from the current study along with our previous work [13,14] clearly show that the surfaces of all the STO samples undergo reconstruction after O_2 treatment at elevated temperatures regardless of the morphology (facet). Such reconstruction

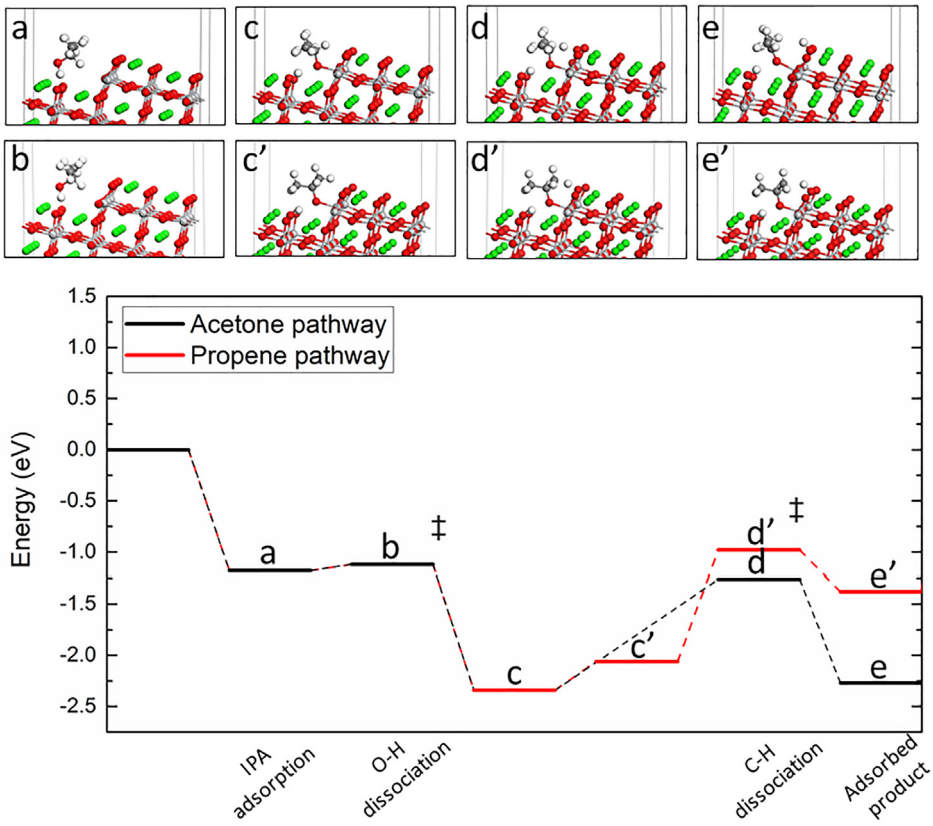

Fig. 11. Energy profile with intermediate and transition state geometries of IPA conversion to acetone (black line) or propene (red line) on the STO (4–10) steps. "‡" indicates the transition state. Elements: Red, O; Green, Sr; Light grey, Ti; Dark grey, C; White, H.

and the surface enrichment of Sr is reflected in the increased acetone selectivity in IPA conversion for the calcined STO over the untreated samples. The increased methane combustion rate over the reconstructed STO [15] was proposed to be from the increase of the reconstructed step sites. In this context, two new insights have been gained from the current work on the reconstruction behaviors of STO perovskite: 1) the step sites from surface reconstruction of STO can be quantified through SSITKA experiment under reaction conditions, and are shown to be the minor sites (<1.4%) on the surface but play the major role in the acid-base conversion of IPA over STO; 2) the degree of surface reconstruction, i.e., the amount of the step sites, can be controlled by not only the pretreatment temperature but also the shape of STO. The temperature effect was shown in both current and previous work [13]: the higher the treatment temperature, the more reconstruction occurs on the STO. Our recent work [14] already indicated there is an impact of surface facet on the surface reconstruction of STO. Such an impact can be quantified by the number of step sites as shown in current study: when the treatment temperature is the same (at 550 °C), the dodecahedra (dominated by (1 1 0)) presents more step sites than the cubes (dominated by (1 0 0)) such that the dodecahedra exhibit a higher IPA conversion rate than the cube. Such facet dependence can be ascribed to the difference in surface energy. The step sites can be more easily created on dodecahedra sample since the (1 1 0) facet is less stable than the (1 0 0) facet on STO cube [57]. Therefore, the facet of STO indirectly tunes the IPA reaction via controlling the degree of surface reconstruction. The implication is that one cannot simply correlate the surface facet (shape) to the catalytic behaviors of oxide catalysts due to the existence of surface reconstruction of most oxides (both single oxides and complex oxides) [58]. This inspires the need to understand the atomic configuration of different facets and the nature of real active sites of oxide nanomaterials under reaction conditions.

It is noted that the density of step sites on the reconstructed truncated STO is the lowest among the three STO shapes after 550 °C treatment although the (1 0 0)/(1 1 0) ratio on the truncated STO is in between the other two shapes, suggesting less surface reconstruction on the truncated STO than both STO cubes and dodecahedra. Such discrepancy could be attributed to two possible causes: (1) the subsurface of truncated STO is different in Sr/Ti composition locally as compared to the other two STO shapes: the truncated sample shows the highest Sr/(Sr + Ti) ratio without thermal treatment (Fig. 2B) in the subsurface region (<1 nm), while it exhibits the lowest Sr/(Sr + Ti) ratio after thermal treatment at 550 °C compared to the other two STO shapes (Fig. 2A). Our previous work indicated that not only the surface composition but also the subsurface Sr/Ti ratio is important for methane conversion (both combustion and oxidative coupling) [15]. We hypothesize this might also work here in the case of IPA conversion. (2) The size of the STO facets may impact the degree of surface reconstruction since reconstruction behaviors of oxides surface could be facet-size dependent [59]. The smaller the facet as in the case of truncated STO, the less reconstruction might occur. It remains an interesting topic that warrants further exploration using STO shapes with varying sizes.

4. Conclusions

The IPA conversion was used as a probe reaction to understand the interplay between surface facet and reconstruction on the catalytic behaviors of $SrTiO_3$ nanocrystals including cube, truncated cube and dodecahedra. Both XPS and low energy ion scattering analysis reveal that the surface reconstruction of all STO samples

depends on both the pretreatment temperature and the shape of STO, leading to the different rate (per surface area) in IPA conversion. The reconstruction-resulted step sites were quantified by the SSITKA study to be a minor portion of all surface sites and are proposed responsible for the acid-base catalysis in IPA conversion over STO. The role of STO facet is to control the degree of surface reconstruction: more step sites occur on less stable (1 1 0) facets, leading to higher overall reaction rate than the (1 0 0) facets. Similarly, higher pretreatment temperature results in a higher degree of reconstruction and thus high density of active step sites, and therefore a higher overall catalytic activity. The reaction mechanism for isopropanol dehydrogenation is proposed based on the *in situ* FTIR investigation and verified by DFT calculations to go through an isopropoxy intermediate adsorbed on the Lewis acid sites present at the surface steps. This work underscores the importance of surface facet on oxide catalysts in controlling the surface reconstruction behaviors and ultimately the catalysis.

Declaration of Competing Interest

The authors declare that they have no known competing financial interests or personal relationships that could have appeared to influence the work reported in this paper.

Acknowledgements

This research is sponsored by the U.S. Department of Energy, Office of Science, Office of Basic Energy Sciences, Chemical Sciences, Geosciences, and Biosciences Division, Catalysis Science program. Part of the work including XRD, SEM and kinetic measurements were conducted at the Center for Nanophase Materials Sciences, which is a DOE Office of Science User Facility. This research used resources of the National Energy Research Scientific Computing Center, a DOE Office of Science User Facility supported by the Office of Science of the U.S. Department of Energy under contract no. DE-AC02-05CH11231.

Notes: This manuscript has been authored by UT-Battelle, LLC under contract No. DE-AC05-00OR22725 with the U.S. Department of Energy. and The United States Government retains and the publisher, by accepting the article for publication, acknowledges that the United States Government retains a nonexclusive, paidup, irrevocable, worldwide license to publish or reproduce the published form of this manuscript, or allow others to do so, for United States Government purposes. The Department of Energy will provide public access to these results of federally sponsored research in accordance with the DOE Public Access Plan (http://energy.gov/downloads/doe-public-access-plan).

Appendix A. Supplementary material

Supplementary data to this article can be found online at https://doi.org/10.1016/j.jcat.2020.02.014.

References

[1] Y.-Y. Pai, A. Tylan-Tyler, P. Irvin, J. Levy, Physics of $SrTiO_3$-based heterostructures and nanostructures: a review, Rep. Prog. Phys. 81 (2018) 036503.
[2] A. Ohtomo, H.Y. Hwang, A high-mobility electron gas at the $LaAlO_3/SrTiO_3$ heterointerface, Nature 427 (2004) 423–426.
[3] Z. Wang, Z. Zhong, X. Hao, S. Gerhold, B. Stoger, M. Schmid, J. Sanchez-Barriga, A. Varykhalov, C. Franchini, K. Held, U. Diebold, Anisotropic two-dimensional electron gas at $SrTiO_3$(110), Proc. Natl. Acad. Sci. USA 111 (2014) 3933–3937.
[4] H. Yan, Z. Zhang, S. Wang, K. Jin, Review of photoresponsive properties at $SrTiO_3$-based heterointerfaces, Chin. Phys. B 27 (2018) 117804.
[5] J.A. Enterkin, W. Setthapun, J.W. Elam, S.T. Christensen, F.A. Rabuffetti, L.D. Marks, P.C. Stair, K.R. Poeppelmeier, C.L. Marshall, Propane oxidation over Pt/$SrTiO_3$ nanocuboids, ACS Catal. 1 (2011) 629–635.
[6] B.-R. Chen, L.A. Crosby, C. George, R.M. Kennedy, N.M. Schweitzer, J. Wen, R.P. Van Duyne, P.C. Stair, K.R. Poeppelmeier, L.D. Marks, M.J. Bedzyk, Morphology and CO oxidation activity of Pd nanoparticles on $SrTiO_3$ nanopolyhedra, ACS Catal. 8 (2018) 4751–4760.
[7] K. Han, T. Kreuger, B. Mei, G. Mul, Transient behavior of Ni@NiOx functionalized $SrTiO_3$ in overall water splitting, ACS Catal. 7 (2017) 1610–1614.
[8] K.E. Sanwald, T.F. Berto, A. Jentys, D.M. Camaioni, O.Y. Gutiérrez, J.A. Lercher, Kinetic coupling of water splitting and photoreforming on $SrTiO_3$-based photocatalysts, ACS Catal. 8 (2018) 2902–2913.
[9] L. Bai, F. Polo-Garzon, Z. Bao, S. Luo, B.M. Moskowitz, H. Tian, Z. Wu, Impact of surface composition of $SrTiO_3$ catalysts for oxidative coupling of methane, ChemCatChem 11 (2019) 2107–2117.
[10] R. Ohshima, Y. Ando, K. Matsuzaki, T. Susaki, M. Weiler, S. Klingler, H. Huebl, E. Shikoh, T. Shinjo, S.T.B. Goennenwein, M. Shiraishi, Strong evidence for d-electron spin transport at room temperature at a $LaAlO_3/SrTiO_3$ interface, Nat. Mater. 16 (2017) 609–614.
[11] Q. Song, H.R. Zhang, T. Su, W. Yuan, Y.Y. Chen, W.Y. Xing, J. Shi, J.R. Sun, W. Han, Observation of inverse Edelstein effect in Rashba-split 2DEG between $SrTiO_3$ and $LaAlO_3$ at room temperature, Sci. Adv. 3 (2017) e1602312.
[12] Z. Ying, S. Chen, T. Peng, R. Li, J. Zhang, Fabrication of an Fe-doped $SrTiO_3$ photocatalyst with enhanced dinitrogen photofixation performance, Eur. J. Inorg. Chem. 2019 (2019) 2182–2192.
[13] F. Polo-Garzon, S.Z. Yang, V. Fung, G.S. Foo, E.E. Bickel, M.F. Chisholm, D.E. Jiang, Z. Wu, Controlling reaction selectivity through the surface termination of perovskite catalysts, Angew. Chem. Int. Ed. Engl. 56 (2017) 9820–9824.
[14] G.S. Foo, Z.D. Hood, Z. Wu, Shape effect undermined by surface reconstruction: ethanol dehydrogenation over shape-controlled $SrTiO_3$ nanocrystals, ACS Catal. 8 (2017) 555–565.
[15] F. Polo-Garzon, V. Fung, X. Liu, Z.D. Hood, E.E. Bickel, L. Bai, H. Tian, G.S. Foo, M. Chi, D.-E. Jiang, Z. Wu, Understanding the impact of surface reconstruction of perovskite catalysts on CH_4 activation and combustion, ACS Catal. 8 (2018) 10306–10315.
[16] C. Ledesma, J. Yang, D. Chen, A. Holmen, Recent approaches in mechanistic and kinetic studies of catalytic reactions using SSITKA technique, ACS Catal. 4 (2014) 4527–4547.
[17] R. Davis, Turnover rates on complex heterogeneous catalysts, AIChE J. 64 (2018) 3778–3785.
[18] J.D. Kammert, J. Xie, I.J. Godfrey, R.R. Unocic, E. Stavitski, K. Attenkofer, G. Sankar, R.J. Davis, Reduction of propionic acid over a Pd-promoted $ReOx/SiO_2$ catalyst probed by X-ray absorption spectroscopy and transient kinetic analysis, ACS Sustainable Chem. Eng. 6 (2018) 12353–12366.
[19] S.I. Shannon, J. James, G. Goodwin, Characterization of catalytic surfaces by isotopic-transient kinetics during steady-state reaction, Chem. Rev. 95 (1995) 677–695.
[20] B.C. McClaine, R.J. Davis, Importance of product readsorption during isotopic transient analysis of ammonia synthesis on Ba-promoted Ru/BaX catalyst, J. Catal. 211 (2002) 379–386.
[21] S. Siporin, Isotopic transient analysis of ammonia synthesis over Ru/MgO catalysts promoted by cesium, barium, or lanthanum, J. Catal. 222 (2004) 315–322.
[22] M. Rotko, A. Machocki, G. Słowik, The mechanism of the CH_4/O_2 reaction on the Pd–Pt/γ-Al_2O_3 catalyst: a SSITKA study, Appl. Catal., B. 160–161 (2014) 298–306.
[23] F. Polo-Garzon, D. Pakhare, J.J. Spivey, D.A. Bruce, Dry reforming of methane on Rh-doped pyrochlore catalysts: a steady-state isotopic transient kinetic study, ACS Catal. 6 (2016) 3826–3833.
[24] J.T. Calla, R.J. Davis, Investigation of alumina-supported Au catalyst for CO oxidation by isotopic transient analysis and X-ray absorption spectroscopy, J. Phys. Chem. B 109 (2005) 2307–2314.
[25] J. Calla, M. Bore, A. Datye, R. Davis, Effect of alumina and titania on the oxidation of CO over Au nanoparticles evaluated by ^{13}C isotopic transient analysis, J. Catal. 238 (2006) 458–467.
[26] J. Schweicher, A. Bundhoo, A. Frennet, N. Kruse, H. Daly, F.C. Meunier, DRIFTS/MS studies during chemical transients and SSITKA of the CO/H_2 reaction over Co-MgO Catalysts, J. Phys. Chem. C 114 (2010) 2248–2255.
[27] J. Yang, E.Z. Tveten, D. Chen, A. Holmen, Understanding the effect of cobalt particle size on Fischer-Tropsch synthesis: surface species and mechanistic studies by SSITKA and kinetic isotope effect, Langmuir 26 (2010) 16558–16567.
[28] A. Carvalho, V.V. Ordomsky, Y. Luo, M. Marinova, A.R. Muniz, N.R. Marcilio, A.Y. Khodakov, Elucidation of deactivation phenomena in cobalt catalyst for Fischer-Tropsch synthesis using SSITKA, J. Catal. 344 (2016) 669–679.
[29] F.A. Rabuffetti, H.S. Kim, J.A. Enterkin, Y.M. Wang, C.H. Lanier, L.D. Marks, K.R. Poeppelmeier, P.C. Stair, Synthesis-dependent first-order Raman scattering in $SrTiO_3$ nanocubes at room temperature, Chem. Mater. 20 (2008) 5628–5635.
[30] F. Polo-Garzon, V. Fung, L. Nguyen, Y. Tang, F. Tao, Y. Cheng, L.L. Daemen, A.J. Ramirez-Cuesta, G.S. Foo, M. Zhu, I.E. Wachs, D.E. Jiang, Z. Wu, Elucidation of the reaction mechanism for high-temperature water gas shift over an industrial-type copper-chromium-iron oxide catalyst, J. Am. Chem. Soc. 141 (2019) 7990–7999.
[31] X. Wang, H. Shi, J. Szanyi, Controlling selectivities in CO_2 reduction through mechanistic understanding, Nat. Commun. 8 (2017) 513.
[32] M. Ocal, R. Oukaci, G. Marcelin, S.K. Agarwal, Steady-State Isotopic Transient Kinetic-Analysis (Ssitka) investigation of no reduction with Co over perovskite catalysts, Ind. Eng. Chem. Res. 33 (1994) 2930–2934.

[33] S.V. Ushakov, A. Navrotsky, Direct measurements of water adsorption enthalpy on hafnia and zirconia, Appl. Phys. Lett. 87 (2005) 164103.
[34] G. Kresse, J. Furthmuller, Efficiency of ab-initio total energy calculations for metals and semiconductors using a plane-wave basis set, Comput. Mater. Sci. 6 (1996) 15–50.
[35] G. Kresse, J. Furthmuller, Efficient iterative schemes for ab initio total-energy calculations using a plane-wave basis set, Phys. Rev. B 54 (1996) 11169–11186.
[36] J.P. Perdew, K. Burke, M. Ernzerhof, Generalized gradient approximation made simple, Phys. Rev. Lett. 77 (1996) 3865–3868.
[37] S. Grimme, J. Antony, S. Ehrlich, H. Krieg, A consistent and accurate ab initio parametrization of density functional dispersion correction (DFT-D) for the 94 elements H-Pu, J. Chem. Phys. 132 (2010) 154104.
[38] P.E. Blöchl, Projector augmented-wave method, Phys. Rev. B 50 (1994) 17953–17979.
[39] H.J. Monkhorst, J.D. Pack, Special points for brillouin-zone integrations, Phys. Rev. B 13 (1976) 5188–5192.
[40] G. Henkelman, B.P. Uberuaga, H. Jónsson, A climbing image nudged elastic band method for finding saddle points and minimum energy paths, J. Chem. Phys. 113 (2000) 9901–9904.
[41] G. Henkelman, H. Jónsson, A dimer method for finding saddle points on high dimensional potential surfaces using only first derivatives, J. Chem. Phys. 111 (1999) 7010.
[42] S.P. Phivilay, A.A. Puretzky, K. Domen, I.E. Wachs, Nature of catalytic active sites present on the surface of advanced bulk tantalum mixed oxide photocatalysts, ACS Catal. 3 (2013) 2920–2929.
[43] G.S. Foo, G. Hu, Z.D. Hood, M. Li, D.-E. Jiang, Z. Wu, Kinetics and mechanism of methanol conversion over anatase titania nanoshapes, ACS Catal. 7 (2017) 5345–5356.
[44] M. Tamura, K.-I. Shimizu, A. Satsuma, Comprehensive IR study on acid/base properties of metal oxides, Appl. Catal., A 433–434 (2012) 135–145.
[45] J.A. Lercher, H. Vinek, H. Noller, Acid–base properties of silica–alumina samples derived from NaX zeolites. Part 1. —Physical characterization and an infrared study of the adsorption of acetone, J. Chem. Soc. Faraday Trans. (1984) 1239–1247.
[46] J. Poth, R. Haberkorn, H.P. Beck, Combustion-synthesis of $SrTiO_3$ Part II. Sintering behaviour and surface characterization, J. Eur. Ceram. Soc. (2000) 715–723.
[47] S.A. Fuente, C.A. Ferretti, N.F. Domancich, V.K. Díez, C.R. Apesteguía, J.I. Di Cosimo, R.M. Ferullo, N.J. Castellani, Adsorption of 2-propanol on MgO surface: a combined experimental and theoretical study, Appl. Surf. Sci. 327 (2015) 268–276.
[48] F. Kooli, C. Martin, V. Rives, FT-IR spectroscopy study of surface acidity and 2-propanol decomposition on mixed oxides obtained upon calcination of layered double hydroxides, Langmuir (1997) 2303–2306.
[49] G. Socrates, Infrared and RAMAN characteristic group frequencies tables and charts, John Wiley & Sons Ltd., Baffins Lane, Chichester, West Sussex PO19 IUD, England, 2004.
[50] G.S. Foo, F. Polo-Garzon, V. Fung, D.-E. Jiang, S.H. Overbury, Z. Wu, Acid-base reactivity of perovskite catalysts probed via conversion of 2-propanol over titanates and zirconates, ACS Catal. 7 (2017) 4423–4434.
[51] S. Tan, M.B. Gray, M.K. Kidder, Y. Cheng, L.L. Daemen, D. Lee, H.N. Lee, Y.-Z. Ma, B. Doughty, D.A. Lutterman, Insight into the selectivity of isopropanol conversion at strontium titanate (100) surfaces: a combination kinetic and spectroscopic study, ACS Catal. 7 (2017) 8118–8129.
[52] R. Rioux, M. Vannice, Dehydrogenation of isopropyl alcohol on carbon-supported Pt and Cu–Pt catalysts, J. Catal. 233 (2005) 147–165.
[53] S. Tan, F. Sayed, S. Yang, Z. Li, J. Wu, P.M. Ajayan, Strong effect of B-site substitution on the reactivity of layered perovskite oxides probed via isopropanol conversion, ACS Materials Lett. 1 (2019) 230–236.
[54] M.A. Petersen, J.-A. van den Berg, I.M. Ciobîcă, P. van Helden, Revisiting CO activation on Co catalysts: impact of step and kink sites from DFT, ACS Catal. 7 (2017) 1984–1992.
[55] I. Kasatkin, P. Kurr, B. Kniep, A. Trunschke, R. Schlogl, Role of lattice strain and defects in copper particles on the activity of Cu/ZnO/Al(2)O(3) catalysts for methanol synthesis, Angew. Chem. Int. Ed. Engl. 46 (2007) 7324–7327.
[56] M.P. Andersson, F. Abild-Pedersen, I.N. Remediakis, T. Bligaard, G. Jones, J. Engbæk, O. Lytken, S. Horch, J.H. Nielsen, J. Sehested, Structure sensitivity of the methanation reaction: H2-induced CO dissociation on nickel surfaces, J. Catal. 255 (2008) 6–19.
[57] K. Huang, L. Yuan, S. Feng, Crystal facet tailoring arts in perovskite oxides, Inorg. Chem. Front. 2 (2015) 965–981.
[58] F. Polo-Garzon, Z. Bao, X. Zhang, W. Huang, Z. Wu, Surface reconstructions of metal oxides and the consequences on catalytic chemistry, ACS Catal. 9 (2019) 5692–5707.
[59] D.A. Bennett, M. Cargnello, B.T. Diroll, C.B. Murray, J.M. Vohs, Shape-dependence of the thermal and photochemical reactions of methanol on nanocrystalline anatase TiO_2, Surf. Sci. 654 (2016) 1–7.